


Ekman-inertial instability

Nicolas Grisouard * and Varvara E. Zemskova *Department of Physics, University of Toronto, 60 St. George Street, Toronto, Ontario, Canada M5S 1A7*

(Received 26 June 2020; accepted 13 November 2020;

published 10 December 2020; corrected 12 May 2021)

We report on an instability arising in subsurface, laterally sheared geostrophic flows. When the lateral shear of a horizontal flow in geostrophic balance has a sign opposite to the Coriolis parameter and exceeds it in magnitude, embedded perturbations are subjected to inertial instability, albeit modified by viscosity. When the perturbation arises from the surface of the fluid, the initial response is akin to a Stokes problem, with an initial flow aligned with the initial perturbation. The perturbation then grows quasi-inertially, rotation deflecting the velocity vector, which adopts a well-defined angle with the mean flow, and viscous stresses, transferring horizontal momentum downward. The combination of rotational and viscous effects in the dynamics of inertial instability prompts us to call this process “Ekman-inertial instability.” While the perturbation initially grows superinertially, the growth rate then becomes subinertial, eventually tending back to the inertial value. The same process repeats downward as time progresses. Ekman-inertial transport aligns with the asymptotic orientation of the flow and grows exactly inertially with time once the initial disturbance has passed. Because of the strongly superinertial initial growth rate, this instability might compete favorably against other instabilities arising in ocean fronts.

DOI: [10.1103/PhysRevFluids.5.124802](https://doi.org/10.1103/PhysRevFluids.5.124802)

I. INTRODUCTION

When wind blows over the ocean surface over long periods of time, momentum diffuses down in a very different manner from Stokes first problem. Instead, the Coriolis acceleration balances downward diffusion of momentum to form Ekman spirals [1]. According to its simplest description [2], horizontal velocity at the surface forms a 45° angle with the direction of the wind and, within the Ekman layer (EL), spirals down to zero over a depth $\sim\sqrt{2\nu/f}$, where ν is the kinematic viscosity (hereafter viscosity), in practice the vertical eddy viscosity, and f is the Coriolis parameter. In spite of its simplicity and notorious difficulty to directly observe in the ocean, this solution has allowed some significant advances in our understanding of ocean dynamics. For example, the predicted cumulative mass transport of ELs provides a relatively accurate explanation of how winds set up ocean gyres (Refs. [1,3] and references therein). Since then, Ekman layer theory has been amended to include weak vorticity effects [4–6], variability of the wind and eddy diffusivity in both space [7] and time [8], or other features of the upper ocean [9].

EL theory has seen a renewed interest in the context of submesoscale studies [10,11]. Submesoscale flows are defined by a vertical vorticity field $\zeta = (\nabla \times \mathbf{v}) \cdot \hat{\mathbf{z}}$ with a magnitude comparable to the planetary vorticity f , i.e., Rossby number of order unity [$\text{Ro} = \zeta/f = O(1)$] [12]. Near the ocean surface, submesoscale flows and their associated vertical velocities could be important for ecosystems [13–15], for atmosphere-ocean exchanges [16,17], and as a kinetic energy sink that could help close the energy budget of the ocean [11,18]. Recent studies have expanded our

*nicolas.grisouard@utoronto.ca

understanding of submesoscale ELs and their impacts by incorporating interactions with $Ro = O(1)$ vortical flows [3], surface waves and Langmuir circulation [9,19], and modifications due to baroclinic pressure torques [9,16,20,21].

In the present study, our goal is to contribute to this effort by describing what we hereafter refer to as “Ekman-inertial instability” (EII), which can be seen as the unstable counterpart of an EL that occurs in anticyclonic flows for which $Ro < -1$. In the oceanic regime, and independent of the results we are about to present, such flows can undergo inertial instability (InI), in which a particle slightly displaced across a geostrophic jet will find itself in a region where the imbalance between ambient pressure gradient and the Coriolis force tends to amplify its displacement [22,23]. The main features of InI are well described by linear stability analysis, i.e., by the growth of a plane-wave-like mode at a rate of $f\sqrt{-1 - Ro}$ in the inviscid limit, constant in time and space.

EII, on the other hand, originates from a change in wind stress at the surface of the ocean, and the vertical extent over which it impacts the fluid increases downward due to viscous stresses, eventually following a typical $\sqrt{\nu t}$ scaling. When $Ro < -1$, it replaces the Ekman layer spin up, which occurs for $Ro > -1$. In the first phase, which we will refer to as “viscous-inertial peeling,” tangential viscous stresses act to set the fluid in motion much faster than the expected exponential growth of InI. In this first phase, the problem is mathematically equivalent to Stokes first (or Rayleigh) problem, albeit for the vertical shear. In particular, in the case of a sudden wind change, it inherits its initially infinite growth rate. Past this initial phase, the flow keeps accelerating in a quasiexponential manner and draws its energy from the lateral shear of the geostrophic current, akin to InI, albeit slowed down by downward diffusion of momentum by viscosity. Originating at the surface, these processes repeat at later times at greater depths.

In the next section, we derive the expressions of the velocity field under EII, followed in Sec. III by a description of how EII physically manifests itself. In Sec. IV, we discuss how EII would insert itself in the dynamical landscape of an unstable front, and in particular, we compare EII with the classical theory of InI in order to predict how they would compete and attempt to predict how EII would play out in a front of finite width. Finally, we offer a summary and conclusions in Sec. V.

II. MATHEMATICAL DESCRIPTION

We present here the solution for the most idealized version of EII. We mirror this derivation with its “stable” counterpart, i.e., the establishment of an EL accompanied by near-inertial oscillations, in the Appendix.

A. Posing the problem

We start with the equations of motion of an incompressible, homogeneous flow, with a traditional f -plane approximation, i.e.,

$$\tilde{\mathbf{v}}_t + \tilde{\mathbf{v}} \cdot \nabla \tilde{\mathbf{v}} + f \hat{\mathbf{z}} \times \tilde{\mathbf{v}} + \nabla \tilde{p} / \rho = \nu \nabla^2 \tilde{\mathbf{v}}, \quad \nabla \cdot \tilde{\mathbf{v}} = 0, \quad (1)$$

where $\tilde{\mathbf{v}} = (\tilde{u}, \tilde{v}, \tilde{w})$ is the full velocity field in a direct Cartesian coordinate system $(\hat{x}, \hat{y}, \hat{z})$, with \hat{z} pointing upward. Subscripts denote partial derivatives, \tilde{p} are the deviations from hydrostatic pressure, and ρ is the constant fluid density.

We next decompose our flow into a component, denoted by bars, that flows in the y direction and is in geostrophic balance with the pressure force in the x direction and deviations from it, namely,

$$\tilde{\mathbf{v}} = \bar{v}(x, z)\hat{y} + (u, v, w), \quad \tilde{p} = \bar{p} + p, \quad \text{such that} \quad f\bar{v} = \bar{p}_x / \rho. \quad (2)$$

The geostrophic balance above neglects viscous diffusion of momentum, which we justify by assuming that the spatial scales of the geostrophic flow are too large for it to act over the timescales of EII. We let the velocity vary in the across-jet direction, which defines a local Rossby number

$$Ro = \bar{v}_x / f. \quad (3)$$

We treat Ro as a constant; that is, we focus on the case of linear lateral shear for \bar{v} : a strong simplification in the submesoscale regime, but one that captures the essential physics of EII. Note that this assumption enforces the geostrophic current's expressions of the form $\bar{v}(x, z) = f\text{Ro}x + \varphi(z)$, where φ is a function of only z . Also note that by treating Ro as a constant, we are effectively setting up an infinite reservoir of energy EII can grow from. We then complete our initial setup by adding boundary conditions at the surface, located at $z = 0$, namely, a rigid lid and an initial wind stress in only the y direction, defined as $T_1^y = \rho v \bar{v}_z|_{z=0}$, such that $\bar{v} = \bar{v}\hat{y}$ is a steady solution of our initial system (1) and the boundary conditions above. The deviations from this initial state, i.e., u , v , w , and p , are initially zero. A change (i.e., an increase, decrease, and/or change in direction) in the wind stress, starting at $t = 0$, will initiate EII.

B. EII derivation

Like in ELs and InI, a constant Ro allows us to ignore all of the horizontal derivatives in the u , v , w , and p fields. Doing so, along with using the incompressibility (1) and the top rigid-lid conditions, yields $w \equiv 0$. Collecting everything, the only remaining advective term in the momentum equations (1) is $\bar{u}\bar{v}_x\hat{y} = f\text{Ro}u\hat{y}$, while all others are exactly zero. The equations of motion (1) then reduce to

$$u_t - fv = vu_{zz}, \quad v_t + (1 + \text{Ro})fu = vv_{zz}, \quad (4)$$

with the other components of Eqs. (1) being trivially satisfied.

EII starts at $t = 0$ with wind stress that evolves as $T^y(t)$, following

$$v_z|_{z=0} = a(t) = [T^y(t) - T_1^y]/(v\rho), \quad t > 0. \quad (5)$$

EL boundary conditions close the system, i.e.,

$$u_z|_{z=0} = 0, \quad \lim_{z \rightarrow -\infty} (u, v) = 0. \quad (6)$$

Note that we could include wind stress in the x direction at a relatively modest analytical cost. The solution would change only quantitatively, and the expressions of the solution would be almost the same as the ones we are about to derive (not shown).

Classically, i.e., for $\text{Ro} > -1$, we would see a transient adjustment, including the radiation of near-inertial waves and/or the spin up of an EL, if $T^y(t)$ were to reach a constant value (we explicitly compute such a case in the Appendix). However, for $\text{Ro} < -1$, EII replaces this adjustment and does not feature either waves or an EL. Instead, as we will show, the flow will grow monotonically.

In order to decouple Eqs. (4), we introduce

$$U = u + v/\alpha, \quad V = -u + v/\alpha, \quad (7)$$

with $\alpha^2 = -1 - \text{Ro}$. In scaled coordinates

$$\tau = Ft, \quad Z = z/\delta, \quad (8)$$

where $F = \alpha f$ and $\delta = \sqrt{2v/F}$, Eqs. (4) become

$$U_\tau - U = U_{ZZ}/2, \quad V_\tau + V = V_{ZZ}/2. \quad (9)$$

Introducing $U^\dagger = Ue^{-\tau}$ in the first equation above reduces it to the mere diffusion equation

$$2U_\tau^\dagger = U_{ZZ}^\dagger, \quad U_Z^\dagger|_{Z=0} = A(\tau)e^{-\tau}, \quad (10)$$

with $A(\tau) = a(\tau)\delta/\alpha$, together with boundary conditions (6). The solution to this system is

$$U^\dagger = \int_0^\tau \frac{A(\tau')e^{-\tau'}}{\sqrt{2\pi(\tau - \tau')}} \exp\left(-\frac{Z^2}{2(\tau - \tau')}\right) d\tau'. \quad (11)$$

After multiplying by e^τ and the change of variables $\theta \mapsto \tau - \tau'$,

$$U = \int_0^\tau \frac{A(\tau - \theta)}{\sqrt{2\pi\theta}} \exp\left(\theta - \frac{Z^2}{2\theta}\right) d\theta. \quad (12)$$

A similar derivation, using $V^\ddagger = Ve^\tau$ instead of $U^\ddagger = Ue^{-\tau}$ in Eq. (9), yields

$$V = \int_0^\tau \frac{A(\tau - \theta)}{\sqrt{2\pi\theta}} \exp\left(-\theta - \frac{Z^2}{2\theta}\right) d\theta, \quad (13)$$

from which we can deduce the solutions to the original Eqs. (4), namely,

$$\begin{bmatrix} u \\ v \end{bmatrix} = \frac{1}{2} \begin{bmatrix} U - V \\ \alpha(U + V) \end{bmatrix} = \int_0^\tau \frac{A(\tau - \theta)}{\sqrt{2\pi\theta}} \begin{bmatrix} \sinh \theta \\ \alpha \cosh \theta \end{bmatrix} \exp\left(-\frac{Z^2}{2\theta}\right) d\theta. \quad (14)$$

The expressions above do not make it immediately clear that the flow represents an instability. This fact will become apparent in the step response to a surface disturbance, which we will derive after we introduce our numerical validation strategy.

C. Validation strategy

To independently validate our findings, we solve Eqs. (4)–(6) in the case of an abrupt change in boundary conditions (constant a and A) with the spectral code Dedalus [24,25]. The depth of our domain is 15δ , and we use 256 Chebyshev modes. We integrate the equations over $15/F$, which is long enough to see EII mature but short enough that it does not reach the bottom of the domain, in agreement with the condition at infinity in Eqs. (6). Because the one-dimensional equations (4) are linear, Dedalus integrates them implicitly in time with a fourth-order Runge-Kutta scheme. At the start of the simulation, u and v vary more strongly. To account for it, we progressively increase the time step from $10^{-5}F^{-1}$ in the beginning, to $10^{-2}F^{-1}$ at infinity, over a duration F^{-1} . However, we did not attempt to optimize the time steps because the integrations complete within seconds on a personal computer.

Simulations shown here are seeded with noise, meaning that EII and InI compete. However, noise-free simulations (not shown) behave virtually identically. As expected from linear calculations, outcomes of numerical simulations and analytical solutions are practically indistinguishable. We present both below for abrupt wind change.

D. Solution following an abrupt wind change

We now focus on the case when wind starts abruptly, i.e., for constant $A(\tau) = A_0$. Note that Eqs. (10) are formally identical to Stokes first (or Rayleigh) problem for U_Z^\ddagger . Therefore, any change in wind stress will imply an infinitely fast adjustment of the vertical shear at the surface, which will later translate into an initially infinite growth rate of EII. Physically speaking, this means that EII will initially respond as fast as the wind evolves, before taking on a life of its own. We numerically tested moderate departures from this case, e.g., an exponential approach to different, constant wind stress values over timescales similar to $1/F$ or shorter, and found behavior qualitatively and quantitatively similar to the abrupt-change case. Should the wind evolve over longer timescales, EII would likely initiate and saturate before said timescales have time to impart their signature on the flow.

Under this condition, Eq. (12) can be cast in the following closed forms:

$$U = \frac{A_0}{\sqrt{2}} \operatorname{Im} \left[e^{Zi\sqrt{2}} \operatorname{erfc} \left(-i\sqrt{\tau} - \frac{Z}{\sqrt{2\tau}} \right) \right] \quad (15a)$$

$$= \frac{A_0}{\sqrt{2}} e^{\tau - Z^2/(2\tau)} \operatorname{Im} \left[\mathcal{W} \left(\sqrt{\tau} + \frac{iZ}{\sqrt{2\tau}} \right) \right], \quad (15b)$$

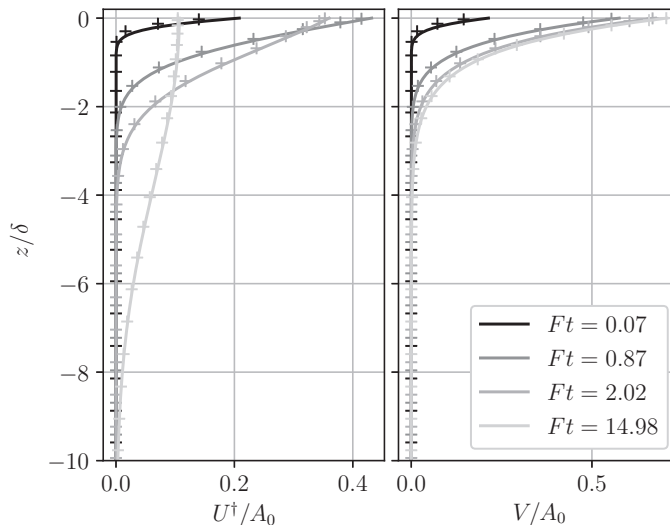


FIG. 1. Evolution of the profiles of U^\dagger and V after an abrupt change in boundary conditions. Solid lines: analytical solutions derived in Sec. II D; crosses: independent numerical integration of Eqs. (4), described in Sec. II C. We display only one cross every eight grid points.

where erfc is the complementary error function, Im denotes the imaginary part, and \mathcal{W} is the Faddeeva function,

$$\forall \xi \in \mathbb{C}, \quad \mathcal{W}(\xi) = e^{-\xi^2} \text{erfc}(-i\xi).$$

We plot U^\dagger corresponding to this solution in Figs. 1 (left panel) and 2 (top panel).

Equation (15b) highlights the long-term behavior of the solution. First, e^τ is the only factor that exhibits a persistently growing behavior, while the rest, namely, U^\dagger , is bounded at all times, which

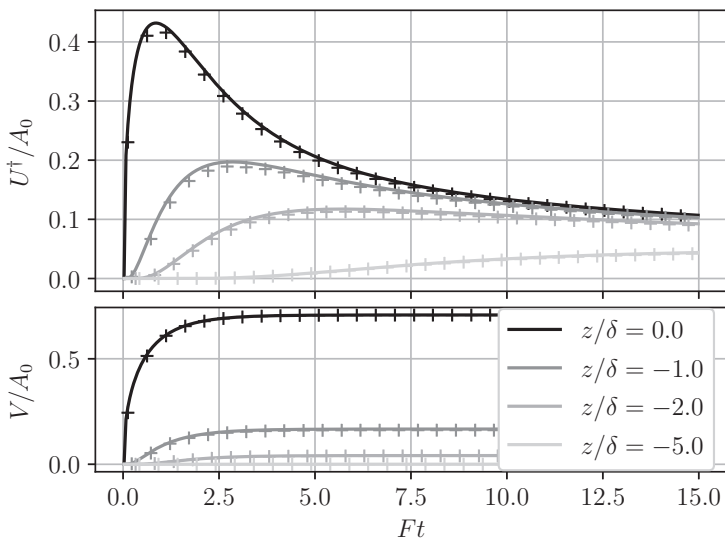


FIG. 2. Same as Fig. 1, presented as time series at a few depths. We display only one cross every ten time steps.

is why we plot only the latter in Figs. 1 and 2. In fact, U grows indefinitely, albeit at a rate that keeps evolving, which we will discuss in Sec. II E. Second, for $\tau \gg 1$, $\mathcal{W}(\dots) \approx \mathcal{W}(\sqrt{\tau})$, and the Z dependence mostly manifests itself in the $e^{-Z^2/(2\tau)}$ factor. Therefore, the bell-shaped profile of U^\dagger found at $Ft \approx 15$ in Fig. 1 is a weakly modulated Gaussian, whose vertical extent scales as $\sqrt{\nu t}$ in dimensional coordinates.

Similarly, Eq. (13) becomes

$$V = \frac{A_0}{2\sqrt{2}} \left[e^{Z\sqrt{2}} \operatorname{erfc} \left(-\sqrt{\tau} - \frac{Z}{\sqrt{2\tau}} \right) - e^{-Z\sqrt{2}} \operatorname{erfc} \left(\sqrt{\tau} - \frac{Z}{\sqrt{2\tau}} \right) \right], \quad (16)$$

which we plot in Figs. 1 (right panel) and 2 (bottom panel). Contrary to U , the error functions above have real arguments, bounding V at all times and depths. In particular, for $\tau \gg 1$, $V \approx A_0/\sqrt{2}e^{Z\sqrt{2}}$ and does not extend deeper than $O(\delta)$.

Figures 1 and 2 show that EII is most pronounced at the surface. There, Eqs. (15) have simple analytical expressions, namely,

$$U|_{Z=0} = \frac{A_0}{\sqrt{2}} \operatorname{erfi}(\sqrt{\tau}) = \sqrt{\frac{2}{\pi}} A_0 e^\tau \operatorname{D}(\sqrt{\tau}), \quad (17a)$$

$$V|_{Z=0} = \frac{A_0}{\sqrt{2}} \operatorname{erf}(\sqrt{\tau}), \quad (17b)$$

where erfi is the imaginary error function and,

$$\forall \xi \in \mathbb{R}, \quad \operatorname{D}(\xi) = \frac{\sqrt{\pi}}{2} e^{-\xi^2} \operatorname{erfi}(\xi)$$

is the Dawson integral. The latter is bounded, with $\operatorname{D}(\sqrt{\tau}) \approx \sqrt{\tau}$ for $\tau \ll 1$, then going through a maximum at $\tau \approx 0.92$, before decaying monotonically to zero, eventually as $1/(2\sqrt{\tau})$.

E. Growth rate

The general expression for the growth rate of U is

$$\sigma_U(t, Z) = \frac{1}{U} \frac{\partial U}{\partial t} = F + \frac{1}{U^\dagger} \frac{\partial U^\dagger}{\partial t}. \quad (18)$$

We hereafter refer to periods of time when $\sigma_U > F$ ($\sigma_U < F$) as ‘‘superinertial’’ (‘‘subinertial’’) in reference to the growth rate of inviscid InI.

The growth rates of U and V can be readily obtained from Eqs. (12) and (13) and the Leibniz integral rule. We explicitly plot σ_U in the case of a sudden wind change in Fig. 3. In accordance with Eq. (18), periods of U^\dagger increasing (decreasing) in Fig. 2 correspond to phases over which U grows superinertially (subinertially). Qualitatively, the growth rate behaves similarly at all depths. Thus, we focus on the surface behavior, which also has the strongest impact on the dynamics of a front. There,

$$\sigma_0 = \sigma_U|_{Z=0} = [2\sqrt{\tau} \operatorname{D}(\sqrt{\tau})]^{-1}, \quad (19)$$

which we can break down following the discussion at the end of Sec. II D. That is, for $\tau \ll 1$, $\sigma_0 \approx 1/(2\tau)$, and the growth rate goes from infinity to unity within a duration $\tau \approx 0.854$. It then decreases and reaches a minimum of $\sigma_0 \approx 0.778F$ at $\tau \approx 2.26$. The growth rate then monotonically increases and asymptotically tends to F .

At depth, the flow qualitatively goes through the same series of steps, with quantitative differences. As Z decreases, the initial growth rate increases in absolute value due to lower values of U . It reaches the $\sigma_U = F$ mark, then its minimum value, which is closer to F at greater depth, at later times.

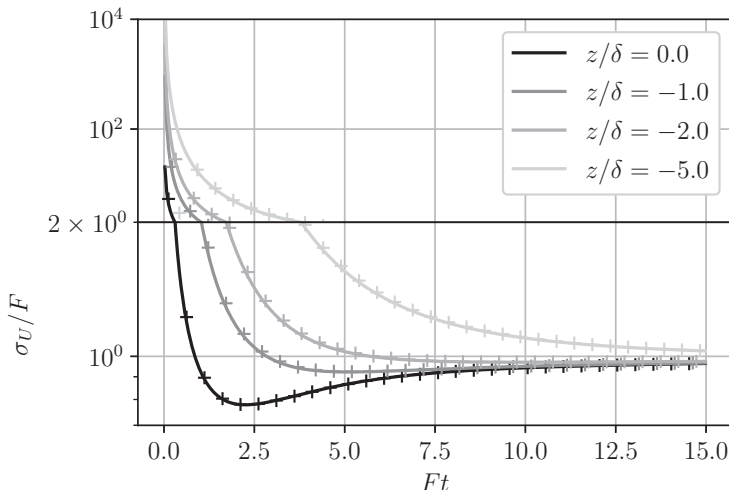


FIG. 3. Same as Fig. 2 for growth rates σ_U . Note the change in the vertical log scale at $\sigma_U = 2F$; curves would appear infinitely differentiable otherwise.

III. INSTABILITY DYNAMICS

This section presents a more qualitative description of EII, namely, the physical mechanisms involved, the morphology of the induced flow, and the implication for mass transport.

A. Dynamics through the lens of energetics

The individual mechanisms involved in EII can be better traced by investigating their energetic signatures. From Eqs. (4), the evolution equation of the kinetic energy density of the flow $K = (u^2 + v^2)/2$ is

$$K_t = -\Pi - \Phi_z - \varepsilon, \quad (20)$$

where $\Pi = \text{Rof}uv$ stands for lateral shear production, i.e., the transfer of kinetic energy from perturbations to the mean shear (negative here); $\Phi = -\nu K_z$ is the viscous diffusive flux of kinetic energy; and $\varepsilon = \nu[(u_z)^2 + (v_z)^2]$ is the irreversible dissipation.

Figure 4 shows that Φ_z plays a role that depends on the phase of EII. In the first phase, which we refer to as “viscous-inertial peeling” (VIP), $-\Phi_z$ is the dominant energy source at the leading edge of the instability, setting the fluid in motion, with $-\Pi$ being the secondary energy source. This phase (Fig. 4, right panel) coincides with the superinertial growth we described in Sec. II E. Near the surface, it lasts $O(F^{-1})$, too short for rotation to influence the dynamics significantly. VIP is therefore a Rayleigh-like problem, with rotation acting as a perturbation.

After the instability front has passed, however (Fig. 4, $z/\delta > -1.5$), $-\Pi$ becomes the dominant source of energy, as in InI, and $-\Phi_z$ acts to reduce the growth of the instability. Physically, rotation is now acting, and the flow set in motion during VIP is inertially unstable, a phase we call “inertial-viscous instability” (InVI). Upper layers of the fluid begin going unstable earlier than lower layers, and their velocity proceeds to grow quasiexponentially. The result is a persistent horizontal momentum imbalance between upper and lower layers, which viscosity diffuses downward. InVI therefore behaves like a viscously dragged InI. As time progresses, EII behaves more and more like inviscid InI: relatively speaking, the vertical gradients diminish (see Fig. 1), Φ_z becomes less important, and the growth rate approaches F .

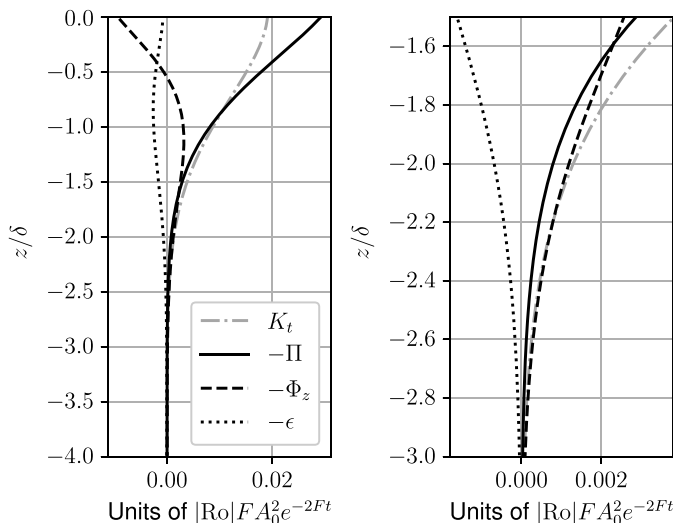


FIG. 4. Kinetic energy budget at $Ft = 2$ [see Eq. (20)]. Both panels display the same data, but the right panel is a magnification of the left panel around the edge of the EII propagation. These plots are of the numerical simulation.

B. Hodograph

EII induces a peculiar velocity field, with some features reminiscent of the Ekman spiral (see Fig. 5), with a caveat that we address in the next paragraph. During the early phases of VIP and near the surface, $e^{\pm\tau} \approx 1$, and Eqs. (12) and (13) show that U and V both initially grow at similar rates. Rotation is not acting yet, and the motion is along the original wind perturbation direction (Fig. 5, left panel). Later, as VIP transitions into InVI near the surface, V settles to a constant value, while U keeps growing quasiexponentially (recall Sec. IID). The near-surface velocity vector therefore

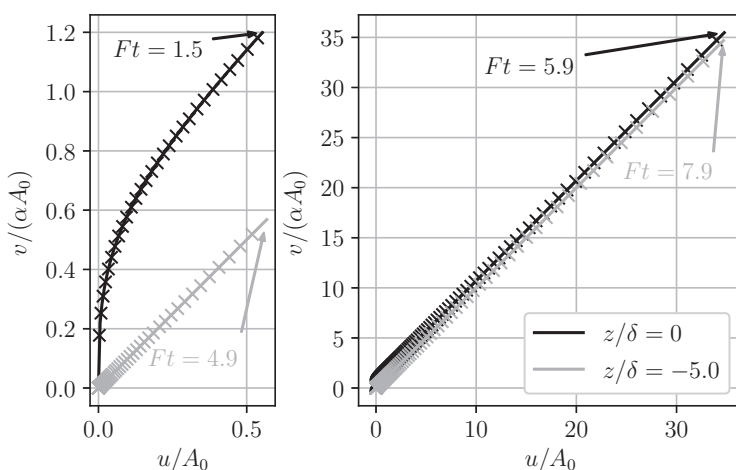


FIG. 5. Scaled hodographs at two different depths as time progresses. Left: short-term behavior. Right: long-term behavior. Annotated arrows indicate the time stamps on the last point of a given line. Solid lines are the theoretical prediction, and crosses are the numerical simulation, with one cross displayed every time step. The axes are scaled equally, showing true angles in $(u, v/\alpha)$ coordinates.

adopts an angle of 45° with the mean flow in $u, v/\alpha$ coordinates (Fig. 5, right panel). For $Z \ll -1$, however, $V \approx 0$ at all times, and the velocity vector adopts this 45° angle immediately (Fig. 5, $z = -5\delta$ lines).

We urge caution, however, in the analogy with ELs: the angle we just mentioned is with the direction of the *mean flow*, not that of the *wind direction*. Indeed, the appearance of this angle traces its roots back to Eqs. (9) and to U and V being the solutions of unstable and stable partial differential equations, respectively. Incorporating a wind disturbance along x in Eq. (6) would change $A(\tau)$ but not the final orientation of the velocity vector.

C. Transport

Contrary to the EL case and its spiraling hodograph, the vertically integrated volume transport due to EII is mostly aligned with the direction of the velocity field. When wind changes abruptly, we have, in EII coordinates,

$$\begin{bmatrix} M^{(U)} \\ M^{(V)} \end{bmatrix} = \delta \int_{-\infty}^0 \begin{bmatrix} U \\ V \end{bmatrix} dZ' = \frac{A_0 \delta}{2} \begin{bmatrix} e^\tau - 1 \\ 1 - e^{-\tau} \end{bmatrix}, \quad (21)$$

or, in across- and along-front coordinates,

$$\mathbf{M} = \begin{bmatrix} M^{(u)} \\ M^{(v)} \end{bmatrix} = A_0 \delta \begin{bmatrix} \cosh \tau - 1 \\ \alpha \sinh \tau \end{bmatrix}. \quad (22)$$

Also note that unlike σ_U , the growth rate of the mass transports reaches F quickly, i.e., over a duration of $O(F^{-1})$.

IV. DISCUSSION

A. Comparison with InI

Unlike many instabilities, the features of EII did not reveal themselves via traditional normal mode analysis. That is, while our initial flow \bar{v}, \bar{p} was the solution of a geostrophic balance and appropriate wind stress at the surface, we did *not* superpose wavelike perturbations, which is traditionally done, for example, for InI, to compute the linear growth rate and determine whether the perturbations may grow. Instead, we added a finite deviation from the top boundary condition by adding some wind stress. In this case, the initial “kick” did not consist of instantiating perturbations in the volume that may or may not grow but resulted from a finite, albeit persistent, change in boundary conditions, which in turn created deviations that may or may not have grown. We also recall that this kick can be any change in wind stress, namely, an increase, a decrease, or a change in direction. We have demonstrated that for $\text{Ro} < -1$, once triggered, the induced flow deviation eventually grows in the runaway fashion that is the hallmark of hydrodynamic instabilities and extracts its energy from the lateral shear of the flow at a rate that eventually converges to that of InI. This similarity in phenomenology, especially when compared to the finite nature of the boundary perturbations, led us to classify this phenomenon as a hydrodynamic instability.

EII exhibits further differences with InI. For InI, $-\Pi$ is the sole source of energy of the unstable perturbations. Velocities grow as part of spatially global wavelike modes, as opposed to the local (i.e., stress-driven) nature of EII expansion. In InI, the viscous flux divergence Φ_z and kinetic energy dissipation ε have passive roles. That is, they are enhanced where InI creates stronger vertical shear and decrease the growth rate everywhere by a constant amount νm^2 , where m is the vertical wave number of the growing mode. Moreover, because $-\Pi$ is not scale selective, InI occurring in a comparable horizontally invariant domain tends to select larger scales to minimize the importance of viscous effects, while the vertical scale of the EII flow constantly increases with $\sqrt{\nu t}$.

Viscosity induces another major practical difference between InI and EII, namely, that a large value of (eddy) viscosity can only prevent the former from growing, while it can aid the latter’s

expansion. Indeed, InI modes grow at a rate $\bar{F} - \nu m^2$, and viscosity's only role is that of damping and scale selection. In EII, however, a larger viscosity has two consequences: (1) it speeds up the vertical propagation of EII via a larger δ , and (2) it decreases its magnitude since $A_0 \propto \nu^{-1/2}$. However, because EII grows fast during VIP, we can reasonably anticipate it will rapidly become detectable even in a highly turbulent environment and impart its signature at depth. Therefore, we argue that regardless of the value of eddy viscosity, EII is likely to always manifest itself, be it as an intense, near-surface current or as a slower, slablike motion of a significant vertical fraction of the front or as some intermediate behavior.

One point of convergence between InI and EII refers to the 45° angle in stretched coordinates between mean and EII flow. Recall, however, that we cautioned in Sec. III B against likening it to the surface deviation from the wind direction of the EL solution. On the other hand, a volume disturbance triggering InI would also induce flow that quickly aligns with the same angle as that of EII by virtue of Eqs. (9), which both EII and InI share.

B. Finite width of currents

As with all instabilities, EII induces a flow that will mix stable and unstable fluids, eventually extinguishing itself. Our solution does not include this effect because we kept Ro , i.e., ζ , constant, effectively providing an endless supply of unstable fluid. In an actual front, however, ζ varies in space. In that case, $M^{(u)}$, the cross-jet volume flux induced by EII, will eventually provoke its extinction: the front is indeed surrounded by stable, $\text{Ro} > -1$, fluid, which would cap the unstable region and stop EII from growing any further.

Furthermore, EII will grow at different rates depending on the location within a front because Ro varies in space. As a consequence, a horizontal velocity divergence u_x will develop, compensated by a vertical velocity divergence w_z , a process called Ekman pumping for ELs. We can compute the vertical velocity w_∞ well below the region where EII occurs by vertically integrating the mass continuity equation, yielding $w_\infty = -M_x^{(u)}$. A comprehensive treatment of the corresponding ‘‘Ekman-inertial pumping’’ will require at least a two-dimensional study, and its complexity will be compounded by the fact that $\text{Ro} = O(1)$, meaning that the x and z directions will be strongly coupled [26]. We defer this study to future work.

V. CONCLUSIONS

Oceanic flows with anticyclonic vertical vorticity that overcompensates planetary vorticity (i.e., $\text{Ro} < -1$) are unstable to perturbations in surface boundary conditions. These perturbations rapidly propagate down via tangential viscous stress, at a rate that far supersedes that of InI if the wind changes rapidly enough, at least initially so. We called this regime viscous-inertial peeling. After the instability is ‘‘primed’’ by the viscous stress, however, the instability behaves like a slightly modified InI. In the simplest possible mathematical description we can make of it, namely, a columnar model, the vertical shear, compensated for inertial exponential growth, essentially follows a Rayleigh problem and inherits its infinite initial growth rate. Assuming an abrupt change in wind conditions allowed us to write closed forms for the solutions and therefore to make some of this behavior more explicit. After VIP, mass transport grows exponentially, at a rate F .

Not only does this instability share several of its features with InI, but the behavior of viscous stresses inevitably brings up features more common to an Ekman spiral superposed with inertial oscillations. In fact, we mirror our derivation to that for the $\text{Ro} > -1$ case in the Appendix, which highlights striking similarities and which prompted us to call this instability Ekman-inertial instability. In particular, the viscous top-down momentum flux is common to both, and its formal ties with the Stokes first problem provide EII with a fast growth rate that may make it competitive with other instabilities such as InI, its baroclinic generalizations within the framework of centrifugal or symmetric instability, and baroclinic instability.

Whether this instability is novel or a mere flavor of InI is up for interpretation. More important, however, is recognizing EII's peculiar behavior, which may manifest itself in peculiar ways in actual ocean fronts. The geostrophic balance above neglects viscous diffusion of momentum, which we justify by assuming that the spatial scales of the geostrophic flow are too large for it to act over the timescales of EII. Investigating more realistic, i.e., two- and three-dimensional configurations, will be the topic of future work. The points we raised in Sec. III C would be a good start, which would raise new questions. In particular, how EII behaves in the presence of vertical and cross-jet buoyancy variations promises interesting discussions. Our one-dimensional model can easily incorporate an evolution equation for the buoyancy fluctuations b , namely,

$$b_t - u\bar{b}_x = \kappa b_{zz}, \quad (23)$$

where \bar{b} is the mean buoyancy field and κ is the buoyancy diffusivity coefficient. For EII to be an instability of the geostrophic flow, thermal wind balance has to apply, namely, $\bar{b}_x = \bar{v}_z/f$. In that case, in order for the initial condition to be a steady solution of the equations of motion, the wind stress has to be $T^y(t < 0) \equiv \rho\nu f\bar{b}_x|_{z=0}$; that is, it has to maintain the surface thermal wind shear, as in previous studies [e.g., 27]. In our one-dimensional model still, b does not feed back into the momentum equations (4). Therefore, EII can advect water masses of different densities across the front, which could directly modify the potential energy of a density front. Grisouard [26] observed that with similar boundary conditions, contrary to predictions from symmetric instability theory, a horizontal flow was advecting buoyancy laterally immediately under the surface and extracting potential energy from the front. Moreover, minimal potential energy exchanges were found between the front and fluctuations when the minimum anticyclonic Rossby number was large, which would have suppressed EII, and the Richardson number of the thermal wind shear was small, which would have favored symmetric instability. At the time, these behaviors had no complete explanations. In light of our results, however, they are consistent with EII out-competing symmetric instability whenever Ro is sufficiently anticyclonic.

Finally, the stability of EII to along-jet and other three-dimensional disturbances such as convection, surface wave effects [28,29], and nontraditional effects [30] should be investigated. Also, the simple viscosity we have used here is only a placeholder for turbulent momentum diffusion, whose effects are far from understood [e.g., 31,32]. We could also include a more complete description of the competition with the transient growth of centrifugal, symmetric, and/or baroclinic instability [33]. One possible avenue is to compare EII with the large-eddy simulations of frontal evolution [34,35]. In particular, Skillingstad *et al.* [34] simplified the dynamics of an unstable submesoscale density filament subjected to varying winds by neglecting all lateral geostrophic gradients and retaining only lateral buoyancy gradients. In their model, sufficiently strong EL and thermal wind shears couple to give rise to an Ekman instability. On the contrary, EII requires a sufficiently strong anticyclonic shear, and it is not directly affected by lateral buoyancy gradients, as we mentioned previously. In a follow-up work [36], the authors add sharp lateral gradients to their front but do not include considerations of the Rossby number. It might be worthwhile to combine both descriptions to obtain more a complete description of submesoscale instabilities.

ACKNOWLEDGMENTS

We acknowledge the support of the Natural Sciences and Engineering Research Council of Canada (NSERC; Grant No. RGPIN-2015-03684) and of the Canadian Space Agency (Grant No. 14SUSWOTTO). We acknowledge fruitful discussions with J. C. McWilliams, which started during the Kavli Institute of Theoretical Physics program on Planetary Boundary Layers in Atmospheres, Oceans, and Ice on Earth and Moons (supported by the National Science Foundation under Grant No. NSF PHY-1748958), with F. Poulin, and with L. N. Thomas. We also acknowledge invaluable input from an anonymous reviewer.

APPENDIX: COMPARISON WITH THE ESTABLISHMENT OF AN EKMAN SPIRAL

When $Ro > -1$, redefining $F = \beta f$, with $\beta = \sqrt{1 + Ro}$, better reveals the setup of an EL. In doing so, Eqs. (8) and (9) apply, albeit with the new definition of F . Note that we do not need to solve for both U and V anymore since u and v derive from the real and imaginary parts of either of them. In line with the traditional presentation of ELs, we solve for $\tilde{V} = u + iv/\beta$ and introduce the counterrotated field $\tilde{V}^\ddagger = \tilde{V} e^{i\tau}$ to obtain the same diffusion equations such as the one in (10), and the counterrotated boundary condition $\tilde{V}_Z^\ddagger|_{Z=0} = iA(\tau)e^{i\tau}$, with $A = v_z|_{z=0}/\beta$. The solution is formally identical to Eq. (13), with the exception of $ie^{-i\theta}$ replacing $e^{-\theta}$. When surface boundary conditions change abruptly,

$$\tilde{V} = \frac{A_0 e^{i\pi/4}}{2\sqrt{2}} \left[e^{Z\sqrt{2}i} \operatorname{erfc} \left(-\sqrt{i\tau} - \frac{Z}{\sqrt{2\tau}} \right) - e^{-Z\sqrt{2}i} \operatorname{erfc} \left(\sqrt{i\tau} - \frac{Z}{\sqrt{2\tau}} \right) \right]. \quad (\text{A1})$$

As $\tau \rightarrow \infty$, $\tilde{V} \rightarrow A_0 e^{Z+i(\pi/4+Z)}/\sqrt{2}$, which is the classical Ekman spiral solution. To obtain this result, we used the identities

$$\frac{e^{i\pi/4}}{\sqrt{2}} \operatorname{erf}(\sqrt{i\tau}) = S(\sqrt{\hat{\tau}}) + iC(\sqrt{\hat{\tau}}) \rightarrow \frac{1+i}{2}, \quad (\text{A2})$$

where S and C are the normalized Fresnel integrals, $\hat{\tau} = 2\tau/\pi$, and the last arrow implies $\lim_{\hat{\tau} \rightarrow \infty}$.

At the surface,

$$\tilde{V}|_{Z=0} = A_0 [S(\sqrt{\hat{\tau}}) + iC(\sqrt{\hat{\tau}})]. \quad (\text{A3})$$

For $\tau \ll 1$, $C(\sqrt{\hat{\tau}}) \approx \sqrt{\hat{\tau}}$, i.e., exhibits a growth rate singularity similar to that of EII. In the other limit $\tau \gg 1$, $C(\sqrt{\hat{\tau}}) - 1/2 \approx \sin \tau / \sqrt{2\pi\tau}$, with S behaving similarly. That is, the convergence to the EL solution manifests itself as near-inertial, or near- F frequency, pseudo-oscillations. Note that their envelope decays as $1/\sqrt{2\pi\tau}$, identical to that of $\sqrt{2/\pi} D(\sqrt{\tau})$, the compensated EII magnitude. The time evolution of the surface hodograph resembles that of a Cornu spiral, albeit one that converges more slowly towards its attractor and with a constant quasifrequency F .

Like EII, this solution highlights two phases: first, that of a rapid adjustment (singular growth rate), followed by a slow ($\sim \tau^{-1/2}$) and oscillatory convergence towards constant values $u/A_0 = v/(\beta A_0) = -1/2$, which is the surface expression of the EL. These two phases are, of course, the stable counterparts to EII's VIP and InVI stages. In fact, because we defined VIP as the phase during which rotation has not affected the motion yet, it appears natural that VIP is shared by both EII and EL.

Contrary to EII, however, a wind disturbance of arbitrary orientation corresponds to a surface boundary condition for \tilde{V}_z that is not purely imaginary and whose phase encodes the disturbance direction. As a result, the orientation of u and v is with respect to the *wind direction*, not the *mean flow*.

-
- [1] G. K. Vallis, *Atmospheric and Oceanic Fluid Dynamics* (Cambridge University Press, Cambridge, 2017).
 - [2] V. W. Ekman, On the influence of the earth's rotation on ocean-currents, *Ark. Mat., Astron. Fys.* **2**, 1 (1905).
 - [3] J. O. Wenegrat and L. N. Thomas, Ekman transport in balanced currents with curvature, *J. Phys. Oceanogr.* **47**, 1189 (2017).
 - [4] M. E. Stern, Interaction of a uniform wind stress with a geostrophic vortex, *Deep Sea Res. Oceanogr. Abstr.* **12**, 355 (1965).
 - [5] P. P. Niiler, On the Ekman divergence in an oceanic jet, *J. Geophys. Res.* **74**, 7048 (1969).
 - [6] Y. Morel and L. N. Thomas, Ekman drift and vortical structures, *Ocean Modell.* **27**, 185 (2009).
 - [7] D. G. Dritschel, N. Paldor, and A. Constantin, The Ekman spiral for piecewise-uniform diffusivity, *Ocean Sci.* **16**, 1089 (2020).

- [8] V. I. Shrira and R. B. Almelah, Upper-ocean Ekman current dynamics: A new perspective, *J. Fluid Mech.* **887**, A24 (2020).
- [9] J. O. Wenegrat and M. J. McPhaden, Wind, waves, and fronts: Frictional effects in a generalized Ekman model, *J. Phys. Oceanogr.* **46**, 371 (2016).
- [10] L. N. Thomas, A. Tandon, and A. Mahadevan, Submesoscale processes and dynamics, in *Ocean Modeling in an Eddy Regime*, edited by M. W. Hecht and H. Hasumi, Geophysical Monograph Series Vol. 177 (American Geophysical Union, Washington, DC, 2008), pp. 17–38.
- [11] J. C. McWilliams, Submesoscale currents in the ocean, *Proc. R. Soc. A: Math. Phys. Eng. Sci.* **472**, 20160117 (2016).
- [12] A strict definition of submesoscale flows would also include a Richardson number that is order 1, i.e., vertical geostrophic velocity gradients that are comparable to the buoyancy frequency of the density stratification. However, we will mostly ignore such effects.
- [13] P. Klein and G. Lapeyre, The oceanic vertical pump induced by mesoscale and submesoscale turbulence, *Annu. Rev. Mar. Sci.* **1**, 351 (2009).
- [14] M. Lévy, P. J. S. Franks, and K. S. Smith, The role of submesoscale currents in structuring marine ecosystems, *Nat. Commun.* **9**, 4758 (2018).
- [15] A. de Verneil, P. J. S. Franks, and M. D. Ohman, Frontogenesis and the creation of fine-scale vertical phytoplankton structure, *J. Geophys. Res.: Oceans* **124**, 1509 (2019).
- [16] J. O. Wenegrat, L. N. Thomas, J. Gula, and J. C. McWilliams, Effects of the submesoscale on the potential vorticity budget of ocean mode waters, *J. Phys. Oceanogr.* **48**, 2141 (2018).
- [17] Z. Su, J. Wang, P. Klein, A. F. Thompson, and D. Menemenlis, Ocean submesoscales as a key component of the global heat budget, *Nat. Commun.* **9**, 775 (2018).
- [18] R. Ferrari and C. Wunsch, Ocean circulation kinetic energy: Reservoirs, sources, and sinks, *Annu. Rev. Fluid Mech.* **41**, 253 (2009).
- [19] J. C. McWilliams, E. Huckle, J.-H. Liang, and P. P. Sullivan, The wavy Ekman layer: Langmuir circulations, breaking waves, and Reynolds stress, *J. Phys. Oceanogr.* **42**, 1793 (2012).
- [20] J. C. McWilliams, J. Gula, M. J. Molemaker, L. Renault, and A. F. Shchepetkin, Filament frontogenesis by boundary layer turbulence, *J. Phys. Oceanogr.* **45**, 1988 (2015).
- [21] M. N. Crowe and J. R. Taylor, The evolution of a front in turbulent thermal wind balance. Part 1. Theory, *J. Fluid Mech.* **850**, 179 (2018).
- [22] T. W. N. Haine and J. Marshall, Gravitational, symmetric, and baroclinic instability of the ocean mixed layer, *J. Phys. Oceanogr.* **28**, 634 (1998).
- [23] B. Cushman-Roisin and J.-M. Beckers, *Introduction to Geophysical Fluid Dynamics*, 2nd ed. (Academic, Cambridge, MA, USA, 2011).
- [24] K. J. Burns, G. M. Vasil, J. S. Oishi, D. Lecoanet, and B. P. Brown, Dedalus: A flexible framework for numerical simulations with spectral methods, *Phys. Rev. Res.* **2**, 023068 (2020).
- [25] See the computer code at <https://github.com/ngrisouard/Ekman-Inertial-Instability>.
- [26] N. Grisouard, Extraction of potential energy from geostrophic fronts by inertial-symmetric instabilities, *J. Phys. Oceanogr.* **48**, 1033 (2018).
- [27] J. R. Taylor and R. Ferrari, On the equilibration of a symmetrically unstable front via a secondary shear instability, *J. Fluid Mech.* **622**, 103 (2009).
- [28] J. C. McWilliams and B. Fox-Kemper, Oceanic wave-balanced surface fronts and filaments, *J. Fluid Mech.* **730**, 464 (2013).
- [29] J. C. McWilliams, Surface wave effects on submesoscale fronts and filaments, *J. Fluid Mech.* **843**, 479 (2018).
- [30] V. Zeitlin, Letter: Symmetric instability drastically changes upon inclusion of the full Coriolis force, *Phys. Fluids* **30**, 061701 (2018).
- [31] P. P. Sullivan and J. C. McWilliams, Frontogenesis and frontal arrest of a dense filament in the oceanic surface boundary layer, *J. Fluid Mech.* **837**, 341 (2018).
- [32] V. Verma, H. T. Pham, and S. Sarkar, The submesoscale, the finescale and their interaction at a mixed layer front, *Ocean Modell.* **140**, 101400 (2019).

- [33] V. E. Zemskova, P.-Y. Passaglia, and B. L. White, Transient energy growth in the ageostrophic Eady model, *J. Fluid Mech.* **885**, A29 (2020).
- [34] E. D. Skillingstad, J. Duncombe, and R. M. Samelson, Baroclinic frontal instabilities and turbulent mixing in the surface boundary layer, part II: Forced simulations, *J. Phys. Oceanogr.* **47**, 2429 (2017).
- [35] H. T. Pham and S. Sarkar, Ageostrophic secondary circulation at a submesoscale front and the formation of gravity currents, *J. Phys. Oceanogr.* **48**, 2507 (2018).
- [36] E. D. Skillingstad and R. M. Samelson, Instability processes in simulated finite-width ocean fronts, *J. Phys. Oceanogr.* **50**, 2781 (2020).

Correction: Two quantities representing the lateral shear production were incorrectly presented after Eq. (20) and have been set right.